HHS Public Access

Author manuscript

Optica. Author manuscript; available in PMC 2018 May 25.

Published in final edited form as:

Optica. 2015 ; 2(2): 169–176. doi:10.1364/OPTICA.2.000169.

Isometric multimodal photoacoustic microscopy based on optically transparent micro-ring ultrasonic detection

Biqin Dong[1,2], **Hao Li**[1], **Zhen Zhang**[2], **Kevin Zhang**[1], **Siyu Chen**[1], **Cheng Sun**[2,*], and **Hao F. Zhang**[1,3,*]

[1]Department of Biomedical Engineering, Northwestern University, Evanston IL 60208

[2]Department of Mechanical Engineering, Northwestern University, Evanston IL 60208

[3]Department of Ophthalmology, Northwestern University, Chicago IL 60611

Abstract

Photoacoustic microscopy (PAM) is an attractive imaging tool complementary to established optical microscopic modalities by providing additional molecular specificities through imaging optical absorption contrast. While the development of optical resolution photoacoustic microscopy (ORPAM) offers high lateral resolution, the acoustically-determined axial resolution is limited due to the constraint in ultrasonic detection bandwidth. ORPAM with isometric spatial resolution along both axial and lateral direction is yet to be developed. Although recently developed sophisticated optical illumination and reconstruction methods offer improved axial resolution in ORPAM, the image acquisition procedures are rather complicated, limiting their capabilities for high-speed imaging and being easily integrated with established optical microscopic modalities. Here we report an isometric ORPAM based on an optically transparent micro-ring resonator ultrasonic detector and a commercial inverted microscope platform. Owing to the superior spatial resolution and the ease of integrating our ORPAM with established microscopic modalities, single cell imaging with extrinsic fluorescence staining, intrinsic autofluorescence, and optical absorption can be achieved simultaneously. This technique holds promise to greatly improve the accessibility of PAM to the broader biomedical researchers.

1. INTRODUCTION

Light microscopy has become an indispensable tool for biological researchers. It has evolved from the ancient “reading stone” to a powerful technology platform that hosts a broad range of imaging modalities for a comprehensive investigation of the physiological processes. The commonly used imaging contrasts include optical scattering, fluorescence, optical absorption, polarization, and various nonlinear optical contrasts such as Raman scattering, etc. Optical scattering imaging is a powerful method to study tissue microanatomy under normal and pathological conditions. For example, in studying pre-cancerous tissue [1,2], optical scattering-based technology relies on the wavelength- and size-dependent scattering

*Corresponding author: c-sun@northwestern.edu & hfzhang@northwestern.edu.

See Supplement Materials **for supporting content**

signatures to quantify intracellular organelle size and architecture variations [3]. However, molecular specificity was not among the strengths of optical scattering-based technologies.

Fluorescence microscopy is considered one of the most powerful and the most sensitive tools for biomedical investigations [4,5]. It allows intrinsic chromophores (such as NAD+ and NADH for cellular metabolism [6]) to be imaged directly or via exogenous labels that are selectively attached to the molecule of interest. Fluorescence microscopy permits single-molecule sensitivity [7] and even nanoscopic resolution [8–10]. It becomes the technique of choice if photobleaching and phototoxicity of the labeling molecules can be tolerated. However, fluorescence microscopy has its limitations. For example, the use of exogenous labels is not always preferred for *in vivo* tissue or cellular imaging [11] and high quantum yield cannot always be achieved [12]. Moreover, additional fluorescent molecules are usually necessities for imaging of nonradioactive nanoparticle-based agents and carriers [13], resulting in more sophisticated synthesis and applications.

In contrast, imaging optical absorption can achieve additional molecular specificity from intrinsic chromophores without labeling [14] and can potentially simplify nanoparticle-based contract agent design [15]. So far, photoacoustic microscopy (PAM) is the only well-investigated technology to quantify optical absorption in three dimensions with high spatial resolutions [16–19]. In PAM, nanosecond laser pulses excite molecules in tissues through linear optical absorption, leading to a transient thermo-elastic expansion and subsequently generating ultrasonic waves with a wide-range of frequency components. This effect is referred to as the photoacoustic (PA) effect. The amplitude of the PA wave reflects optical energy deposition, which is the product of the local optical absorption coefficient and optical fluence. As a result, a PAM image reveals the volumetric distribution of optical absorption.

Despite the prior success of PAM in investigating a wide range of physiological processes, such as blood flow [20,21], oxygen metabolism [22,23], tumor progression [24], and brain activities [25], PAM systems are not easily accessible by the vast majority of biomedical researchers. So far, PAM is not currently commercially available to be used in a way similar to established optical microscopic modalities. Existing PAM systems usually use piezoelectric transducers for ultrasound detection, offering an easy access, low cost, and high sensitive at the expense of a limited ultrasonic detection bandwidth. However, sizeable and optically opaque piezoelectric detectors require a rather large clearance between the sample and the objective lens to accommodate these piezoelectric detectors. As a result, only an objective lens with a large working distance, but low numerical apertures (NAs) can be used. Such a limitation not only imposes constraints in the spatial resolution of PAM, but more importantly, it prevents a practical integration of PAM with established microscopic modalities that require high NAs, such as two-photon microscopy. Several attempts have been made to integrate PAM with confocal microscopy [26–29]. Co-recognized images can be obtained under reflection configuration by adding an acoustic reflector for redirecting PA signals [26] or inserting a needle-type transducer [27,28] between objective lens and sample. The lateral resolution was limited to several microns since the required long working distance limits the NA of objective lens being used. In contrast, high resolution integrated PAM can be realized under transmission configuration [29], however, samples thickness are limited. Furthermore, the implement of isometric three-dimensional PAM, acquiring the

volumetric imaging with comparable axial and lateral resolutions, is restricted by the poor acoustically determined axial resolution due to the finite operational bandwidth of the detectors, unless sophisticated optical illumination and reconstruction are employed [30–32].

Recent studies have shown that optical detection of ultrasonic waves has several advantages over traditional piezoelectric detection, especially for PAM to overcome the aforementioned difficulties, as well as to achieve high axial resolution (requiring a much larger ultrasonic detection bandwidth comparing with that of piezoelectric detectors) and to minimally impact an independent optical microscopy system [33]. We recently developed an optically-transparent, micro-ring resonator (MRR)-based ultrasonic detector (diameter < 100 μm) and fabricated it on a microscope coverslip (thickness: 225 μm) [34]. Such a miniaturized ultrasonic detector meets the strict dimension requirements for seamlessly integrating PAM with optical microscopic modalities using high NA objective lenses. In addition, the MRR ultrasonic detector provides a high ultrasonic detection sensitivity (noise equivalent pressure: 6.8 Pa), a wide angular detection range (7 degrees at 200 MHz), and large ultrasonic detection bandwidth (280 MHz at −6 dB) [34]. Here, we demonstrated a multimodal microscopic system developed around a commercial inverted microscopic platform to achieve ultrahigh-resolution, isometric PAM imaging of single red blood cells and the simultaneous autofluorescence, fluorescence labeling, and optical absorption imaging of retinal pigment epithelium.

2. OPTICAL MULTIMODAL MICROSCOPIC SYSTEM

The schematic and working principle of our multimodal system is shown in Fig. 1. We integrated the MRR ultrasonic detector into a commercial inverted optical microscope body (IX81, Olympus) [Fig. 1(a)]. We used two lasers in the system: a 532-nm Nd:YAG nanosecond pulsed laser (10-nJ per pulse energy, 1-ns pulse duration, Elforlight) as both the PAM excitation and one fluorescence excitation source and a 488-nm continuous wave (CW) Argon-ion laser (161C-410-21, Spectra-Physics) as the second fluorescence excitation source. Both lasers were spatially filtered using 25 μm pinholes (PH1 and PH2) and then combined through a set of dichroic mirrors (DM1, DM2, and DM3, 560, 500 and 525 nm long-pass filters, respectively). A dual-axis galvo-mirror assembly (Nutfield Technology) was used to scan the laser beam and a matching 1:3 Keplerian telescope (KT) further coupled the laser beam to the back aperture of the objective lens (Olympus, 20×, NA 0.45) through the side port of the microscope body. The magnification ratio of the telescope was adjusted to allow the laser beam to overfill the back aperture slightly in order to produce a diffraction-limited focus on the specimen (see method of sample placement in Supplementary Material).

In the integrated PAM sub-system, the detection of the PA signal was accomplished by using a MRR detector mounted at the center of the microscope stage [see the magnified inset in Fig. 1(a)]. A narrow-band tunable laser (765–781 nm, TLB-6712, New Focus) was coupled to the MRR using a single mode optical fiber to excite the whispering gallery mode (WGM). Transmitted light from the MRR device was recorded by a low noise, high-speed avalanche photodetector (APD210, Menlo Systems, 5 MHz to 1 GHz bandwidth). The detected signals were further amplified by an amplifier (AMP, ZFL500NL+, Mini-circuits, 10 MHz to a 500

MHz bandwidth) and digitized by a digitizer (3 GS/s sampling rate, 1.5 GHz bandwidth, CobraMax, GaGe). The measured sensitivity of the MRR ultrasonic detector is 47.1 V/MPa with a noise equivalent pressure of 6.8 Pa and a dynamic range of 2 MPa [34]. During imaging, the pulsed laser and the galvo-mirrors were synchronously triggered by analog signals generated from a computer (PC). The pulse-to-pulse laser amplitude was monitored by a photodiode (PD, DET10A, Thorlabs) to provide the synchronization trigger (ST) for data acquisition (DAQ), as well as a reference to compensate for the intensity fluctuation of PAM. The time-resolved PA signals were converted to depth-resolved A-lines, allowing reconstruction of a three-dimensional (3D) image from a two-dimensional (2D) optical scan [17]. Therefore, an image consisting of 256×256 A-lines can be acquired in 6.6 s at 10 kHz pulse repetition rate.

We integrated a simultaneous dual-channel confocal fluorescent microscopy with the optical-scanning PAM. In the confocal sub-system, the fluorescent signals were obtained through the same objective lens as in the PAM and then separated by a set of dichroic mirrors (DM1 and DM3) and filters (BF and LPF, 520 band-pass filter and 550 nm long-pass filter, respectively). The collected dual-channel fluorescent signals were filtered individually by two 20 μm confocal pinholes (PH3, 4) to reject out-of-focus components. The fluorescent signals were detected by two photodetectors (PMT, Hamamatsu, and APD 110, Thorlabs) and digitized by a second DAQ board (200 MS/s sampling rate, CS14200, Gage). The multichannel fluorescence modalities share the common optical scanning and delivery mechanism with PAM, which permits simultaneous multi-modality and naturally registered images. During the alignment, the built-in Halogen lamps were used as the illumination sources, and we can observe the sample from the wide-field microscope.

3. PERFORMANCE OF PAM USING MICRO-RING BASED ULTRASONIC DETECTOR

The working principle of this MRR-based PAM is illustrated in Fig. 1(b). The MRR ultrasonic detector consists of a polymeric micro-ring waveguide with a diameter of 60 μm and a matching bus waveguide fabricated on a 225-μm-thick quartz microscope coverslip (see fabrication details in Supplementary Material). It can be easily fit into the tight space between the sample and the high-NA objective lens. The incident short pulse laser can be focused through the transparent MRR ultrasonic detector onto the sample. The laser-induced PA waves are then detected by the MRR ultrasonic detector. Figure 1(c) shows a typical resonance spectrum at the critical coupling condition and its Lorenz fitting indicating the corresponding quality factor (Q-factor) of 10^4. The generated PA wave deforms the polymeric MRR waveguide [Fig. 1(c), inset] and subsequently changes the effective optical path length of the corresponding WGM. The change of path length results in a shift in the resonant frequency [dashed red line in Fig. 1(c)] that can be quantified by monitoring the modulation of the transmitted optical intensity through the bus waveguide using a narrowband laser source. Under the weak perturbation approximation, the measured intensity modulation is believed to be proportional to the optical absorption of the tissue [35].

Using such an optically-transparent MRR ultrasonic detector offers several advantages. First, an optical based detection exhibits a much broader frequency response, which is beneficial for obtaining high axial resolution in PAM. Moreover, MRR ultrasonic detector can provide a larger field of view in laser-scanning PAM due to its wide angular detection range [36] at high frequencies (7 degrees with an ultrasonic detection bandwidth of 200 MHz, see details in Supplementary Material). Secondly the ultrasonic detector can be placed at the center of the optical field of view to ensure the optimal sensitivity for ultrasonic detection. Thirdly, such a thin coverslip-style detector is fully compatible with existing optical microscopy modalities, reducing the need for modifying the existing microscopic systems. These advantages potentially offer the possibility to directly modify existing optical microscopic systems already in the labs and adding the capability of PAM for the multimodality microscopy.

We quantified the lateral resolution of this PAM using artificial samples by imaging the micro-pattern fabricated on a 1.5-μm-thick carbon black (CB) thin film by E-beam lithography (Fig. S2). The edge spread function (ESF) was recorded by linearly scanning the edge of the CB thin film, and the corresponding line spread function (LSF) was obtained by taking the first derivative of the ESF [see Fig. S3(a) and S3(b)]. The full-width-half-maximum of the LSF indicates a lateral resolution of 0.73 μm, which is close to the corresponding theoretical diffraction limit. The result suggests that placing our optically-transparent ultrasonic detector directly in the optical path did not affect the optical focus of the imaging system much. We also imaged a commercial resolution target (USAF-1951, Applied Image) and the smallest group of bars (group 7, element 6, bar width 2.19 μm) can be well resolved [see Fig. S2(c)].

We estimated PAM's axial resolution through a typical time-resolved PA signal [Fig. 1(d)] acquired from the CB thin film. The Fourier transform of the time-resolved signal yields a detection bandwidth up to 280 MHz [−6dB, Fig. 1(e)], which is fundamentally limited by the frequency dependent ultrasonic attenuation in water [37]. The convolution of measured PA impulse responses and its time-shifted waveform was calculated using the Hilbert transformation (Fig. S3). We used the minimal time delay for two convoluted impulses remaining distinguishable at a contrast-to-noise ratio of 6-dB to estimate the axial resolution. Using the current MRR detector, our PAM's axial resolution is 2.12 μm, which is solely determined by the ultrasonic detection bandwidth and it is better than the optical depth of field of the objective lens used in the experiment (~5.25 μm, see Supplementary Material for more details). The reflection of PA waves from the substrate can be separated in time domain unless the sample-substrate distance is less than the axial resolution provided by the MRR ultrasound detector (see Fig. S6). Additionally, an acoustic matching layer (e.g. polyimide film) can be further coated on the glass substrate to minimize the effect of reflection [38] and add a necessary time delay of the reflected acoustic signal.

Clearly, employing high NA objective lenses enables PAM a sub-micrometer lateral resolution to image samples at the cellular level. We demonstrated this capability by imaging healthy mouse red blood cells (RBCs). So far, existing PAM cannot resolve the complete profile of a single RBC in 3D due to limited axial resolution [18]. Figure 2(a) and 2(b) show the trans-illuminated optical and PAM images of a mouse blood smear, respectively. The

biconcave shape of the cell can be identified in both images. A magnified PAM projection image (along the *x*-*y* plane) of a single RBC is shown in Fig. 2c and a cross-sectional view of the RBC at the position highlighted by the arrows in Fig. 2(d), where the biconcave disk shape of the RBC can be resolved more clearly. A volumetric rendering of a single RBC in 3D [Fig. 2(e)] visualizes its biconcave shape further (see Video S1 in Supplementary Material). Based on PAM imaging results, the thickness of a single RBC along the *y*-*z* plane is estimated to be 3.84 μm. This demonstrates a practicable determination of a single RBC's morphology and pathology from their size, shape, and intrinsic optical absorption properties by high-resolution isometric PA imaging utilizing MRR ultrasonic detector.

4. SIMULTANEOUS MULTIMODAL IMAGING OF RETINAL PIGMENT EPITHELIUM

To demonstrate the multimodal imaging capability, we imaged retinal pigment epithelium (RPE) cells with three different contrasts. The RPE is a monolayer of pigmented cells located between the choriocapillaris and light-sensitive outer segments of the photoreceptors [39]. Usually, distinct parts of the RPE, such as cytokeratin, tubulin and nuclei, can be distinguished under fluorescence microscopy after being stained with various fluorescence labels. Melanin and lipofuscin granules are two major natural pigment granules in RPE cells. Melanin, acting as an antioxidant for protecting RPE cells from oxidative damage, may lose its function with aging and also can be irreversibly photobleached as a result of long-duration or strong light exposure [40]. On the other hand, lipofuscin is a by-product of phagocytosis of the photoreceptor outer segments, which accumulates with the aging of the retina. Excessive levels of the lipofuscin accumulation exhibit toxic responses to light irradiation compromising essential RPE functions [41] and correlated with the pathogenesis of age-related macular degeneration (AMD). AMD is among the foremost major concerns in ophthalmology, as it is the primary cause for irreversible vision loss worldwide. Although *In vivo* studies of melanin concentration in the retina using PAM with needle-type piezoelectric transducer (35 MHz center frequency) was previously demonstrated [42,43], the imaging resolution can be affected by acoustic attenuation caused by large source-detector separation. Since several physiological processes can be investigated using RPE flat mount, e.g. blue light induced pigment variation [44], *ex vivo* retinal imaging (with higher spatial resolution) may bridge the gap between histology and *in vivo* fundus imaging.

The ability for simultaneously demarcating individual RPE cells and quantifying distributions of lipofuscin and melanin as well as their intracellular content ratios can be critical to uncover and the role of photic stress in predisposing to AMD [41]. The integrated PAM and confocal microscopy is well suited to address this need. The RPE melanin provides an ideal optical absorption imaging contrast within a wide optical spectral range for PAM and lipofuscin is currently been quantified by its strong autofluorescence. When excited at 532 nm, the autofluorescence emission spectral range of lipofuscin is from 580 nm to 700 nm [42]. In addition to these two intrinsic contrasts, we used an F-actin-specific marker (Alexa Fluor 488-Phalloidin) to label the actin filaments to highlight the boundaries of individual RPE cells. The Phalloidin dye has an excitation maximum around 488 nm and an emission maximum around 518 nm, which do not overlap with the absorption and

emission bands for lipofuscin. Thus, we can image all the three optical contrasts simultaneously using two excitation sources at 532 nm and 488 nm.

Figure 3 shows the multimodal imaging of a normal human RPE flat mount (age of the donor: 79 years, see preparation method in Supplementary Material). The 2D PAM projection image is shown in Fig. 3(a), where the false-color of each image pixel represents the local melanin concentration. The individual RPE cells are well defined as close-packed hexagons in the PAM image. As most of the melanosome are usually evenly distributed inside RPE cells in healthy eyes, the RPE cells appear roughly homogeneous in the PAM image with dark boundaries. A cross-sectional view of the imaged RPE layer is shown in Fig. 3(b), which suggests an average thickness of about 8 μm. A 3D rendering is shown in Fig. 3(c) and a video showing visualization of the imaged RPE cells from different angles is provided in the Supplementary Material. The morphology of the RPE cells imaged by PAM agrees with fluorescence microscopy imaging of the labeled actin, which specifically highlights the RPE cell boundary [Fig. 3(d)]. Figure 3(e) shows the autofluorescence image that indicates a higher concentration of lipofuscin near the RPE cell boundary while modest amount of lipofuscin exist within the cell [45]. As all three images are naturally registered, overlaying them provides an improved visualization of the cell morphology and intracellular melanin and lipofuscin distributions as shown in Fig. 3(f).

Visualizing high-resolution 3D tomography of single RPE cells and distributions of chemical by-products demonstrate the developmental potential of this technology towards pathological studies for patients with RPE-related retinopathies. Furthermore, the promising improvements of the spatial resolution in PAM offer a possibility to further investigate the concentration and topographical distribution of melanin granules at the cellular level and beyond. Such a capability is currently not available from any other optical modalities.

5. DISCUSSION

We believe that the much degraded axial resolution (in comparing with its lateral resolution) in PAM greatly affects its capability to be integrated with well-established commercial optical microscopy modalities. In standard optical imaging modalities, axial resolution usually relies on the depth of optical focus, which can be improved by using a confocal pinhole to reduce the effect of diffraction on image formation. In PA imaging, axial information is carried by time-resolved PA signals; hence the determination of its axial resolution, which is different from optical microscopy, mostly relies on the bandwidth of ultrasonic. Although it is possible to realize optical sectioning in PAM by applying pump-probe style illumination [30,31] or multi-view deconvolution of B-scans taken from multiple orientations to improve the axial resolution [32], these systems tend to be overly complicated and lack practicality in high-speed imaging acquisition. In our MRR ultrasonic sensor, the detection bandwidth, determined by the temporal response of optical resonance and the propagation of ultrasonic waves, can potentially reach beyond 1 GHz [34]. It may offer a sub-micron axial resolution and the capability of distinguishing details within the depth of optical focus permitted by ultrasonic attenuation. In addition, the extended detection saturation limit can further improve the accuracy of PA functional imaging [34].

To implement our MRR ultrasonic detector to existing optical microscopy platforms may bring PAM to the broader biomedical research community at much reduced extra costs. The mass production of MRR ultrasonic detectors by employing well-established e-beam lithography or nano-imprinting methods [46] provides lower unit cost and higher quality stability. Despite the side cost from a narrow linewidth laser and a low-noise high-sensitive photodetector, the overall cost is still considerably less than redesigning a microscopy platform solely for PAM. In the future, it is possible to fabricate and integrate both the operation laser and on-chip photodetectors on the “smart coverslip”.

6. CONCLUSION

The use of the transparent MRR ultrasonic detector offers unique advantages in ultrasonic detection that enables an isometric three-dimensional imaging of optical absorption contrast in biological tissue. It features high sensitivity, low detection limits, wide directivity, and an ultra-broadband frequency response. The convenient integration of this miniaturized detector with other imaging modalities, including optical confocal microscopy, two-photon microscopy and optical coherence tomography, may lead to many prospective applications of complementary high-resolution imaging in biomedical research including cancer research, neuroscience and ophthalmology, as well as clinical diagnostics including cancer, hemopathy, and age-related macular degeneration.

Supplementary Material

Refer to Web version on PubMed Central for supplementary material.

Acknowledgments

We thank Dr. Kevin Jia and Mrs. Julie Ives from Olympus for their technical and experimental supports.

Funding Information

National Institutes of Health (1R01EY019951 and 1R24EY022883); National Science Foundation (CBET-1055379, BDI-1353952, CBET-1066776, CMMI-0955195, and CMMI-0751621)

References

1. Backman V, Wallace MB, Perelman LT, Arendt JT, Gurjar R, Müller MG, Zhang Q, Zonios G, Kline E, McGilligan JA, Shapshay S, Valdez T, Badizadegan K, Crawford JM, Fitzmaurice M, Kabani S, Levin HS, Seiler M, Dasari RR, Itzkan I, Van Dam J, Feld MS, McGillican T. Detection of Preinvasive Cancer Cells *In Situ*. Nature. 2000; 406:35–36. [PubMed: 10894529]
2. Perelman LT, Backman V, Wallace M, Zonios G, Manoharan R, Nusrat A, Shields S, Seiler M, Lima C, Hamano T, Itzkan I I, Van Dam J, Crawford JM, Feld MS. Observation of periodic fine structure in reflectance from biological tissue: a new technique for measuring nuclear size distribution. Phys. Rev. Lett. 1998; 80:627–630.
3. Perelman L. Optical diagnostic technology based on light scattering spectroscopy for early cancer detection. Expert Rev. Med. Dev. 2006; 3:787–803.
4. Denk W, Strickler JH, Webb WW. Two-photon laser scanning fluorescence microscopy. Science. 1990; 248:73–76. [PubMed: 2321027]
5. Eigen M, Rigler R. Sorting single molecules – application to diagnostics and evolutionary biotechnology. Proc. Nati. Acad. Sci. 1994; 91:5740–5747.

6. Belenky P, Bogan KL, Brenner C. NAD+ metabolism in health and disease. Trends Biochem. Sci. 2007; 32:12–19. [PubMed: 17161604]
7. Weiss S. Fluorescence spectroscopy of single biomolecules. Science. 1999; 283:1676–1683. [PubMed: 10073925]
8. Hell SW. Far-field optical nanoscopy. Science. 2007; 316:1153–1158. [PubMed: 17525330]
9. Zhuang XW. Nano-imaging with STORM. Nat. Photonics. 2009; 3:365–367. [PubMed: 20300445]
10. Betzig E, Patterson GH, Sougrat R, Lindwasser OW, Olenych S, Bonifacino JS, Davidson MW, Lippincott-Schwartz J, Hess HF. Imaging intracellular fluorescent proteins at nanometer resolution. Science. 2006; 313:1642–1645. [PubMed: 16902090]
11. Jing C, Cornish VW. Chemical tags for labeling proteins inside living cells. Accounts Chem. Res. 2011; 44:784–792.
12. Resch-Genger U, Grabolle M, Cavaliere-Jaricot S, Nitschke R, Nann T. Quantum dots versus organic dyes as fluorescent labels. Nat. Methods. 2008; 5:763–775. [PubMed: 18756197]
13. Yavuz MS, Cheng Y, Chen J, Cobley CM, Zhang Q, Rycenga M, Xie J, Kim CH, Song KH, Schwartz AG, Wang LV, Xia Y. Gold nanocages covered by smart polymers for controlled release with near-infrared light. Nat. Materials. 2009; 12:935–939.
14. Wang LV, Hu S. Photoacoustic tomography: In vivo imaging from organelles to organs. Science. 2012; 335:1458–1462. [PubMed: 22442475]
15. Kim C, Cho EC, Chen J, Song KH, Au L, Favazza C, Zhang Q, Cobley CM, Gao F, Xia Y, Wang LV. In vivo molecular photoacoustic tomography of melanomas targeted by bio-conjugated gold nanocages. ACS Nano. 2010; 4:4559–4564. [PubMed: 20731439]
16. Zhang HF, Maslov K, Stoica G, Wang LV. Functional photoacoustic microscopy for hi-resolution and noninvasive in vivo imaging. Nat. Biotech. 2006; 24:848–851.
17. Zhang HF, Maslov K, Wang LV. In vivo imaging of subcutaneous structures using functional photoacoustic microscopy. Nat. Protoc. 2007; 2:797–804. [PubMed: 17446879]
18. Hu S, Maslov K, Wang LV. Three-dimensional optical-resolution photoacoustic microscopy. J. Vis. Exp. 2011; 3:2729.
19. Mehrmohammadi M, Yoon SJ, Emelianov SY. Photoacoustic imaging for cancer detection and staging. Current Molecular Imaging. 2013; 2:89–105. [PubMed: 24032095]
20. Zhou Y, Liang J, Maslov KI, Wang LV. Calibration-free *in vivo* transverse blood flowmetry based on cross correlation of slow time profiles from photoacoustic microscopy. Opt. Lett. 2013; 38:3882–3885. [PubMed: 24081077]
21. Song W, Liu W, Zhang HF. Laser-scanning Doppler photoacoustic microscopy based on temporal correlation. Appl. Phys. Lett. 2013; 102:203501. [PubMed: 23825803]
22. Liu T, Wei Q, Wang J, Jiao SL, Zhang HF. Combined photoacoustic microscopy and optical coherence tomography can measure metabolic rate of oxygen. Biomed. Opt. Express. 2011; 2:1359–1365. [PubMed: 21559147]
23. Chatni MR, Xia J, Sohn R, Maslov K, Guo Z, Zhang Y, Wang K, Xia Y, Anastasio M, Arbeit J, Wang LV. Tumor glucose metabolism imaged *in vivo* in small animals with whole-body photoacoustic computed tomography. J. Biomed. Opt. 2012; 17:076012. [PubMed: 22894495]
24. Yao J, Maslov KI, Wang LV. *in vivo* photoacoustic tomography of total blood flow and potential imaging of cancer angiogenesis and hypermetabolism. Technol. Cancer Res. T. 2012; 11:301–307.
25. Yao J, Xia J, Maslov K, Naziriavanaki M, Tsytsarev V, Demchenko AV, Wang LV. Noninvasive photoacoustic computed tomography of mouse brain metabolism *in vivo*. NeuroImaging. 2013; 64:257–266.
26. Wang Y, Maslov K, Kim C, Hu S, Wang LV. Integrated photoacoustic and fluorescence confocal microscopy. IEEE Trans. Biomed. Eng. 2010; 57:2576–2578. [PubMed: 20639165]
27. Zhang X, Jiang M, Fawzi AA, Li X, Shung KK, Puliafito CA, Zhang HF, Jiao S. Simultaneous dual molecular contrasts provided by the absorbed photons in photoacoustic microscopy. 2010; 35:4018–4020.
28. Jiao, S., Zhang, HF. Multimodal Microscopy for Comprehensive Tissue Characterizations. In: Wang, RK., Tuchin, VV., editors. Advanced Biophotonics: Tissue Optical Sectioning. Taylor & Francis: 2013.

29. Rao B, Soto F, Kerschensteiner D, Wang LV. Integrated photoacoustic, confocal, and two-photon microscope. J. Biomed. Opt. 2014; 19:36002. [PubMed: 24589986]
30. Shelton RL, Applegate BE. Ultrahigh resolution photoacoustic microscopy via transient absorption. Biomed. Opt. Express. 2010; 1:676–686. [PubMed: 21258499]
31. Yao J, Wang L, Li C, Zhang C, Wang LV. Photoimprint photoacoustic microscopy for three-dimensional label-free subdiffraction imaging. Phys. Rev. Lett. 2014; 112:014302. [PubMed: 24483902]
32. Zhu L, Li L, Gao L, Wang LV. Multiview optical resolution photoacoustic microscopy. Optica. 2014; 1:217–222. [PubMed: 25558469]
33. Beard PC. Biomedical Photoacoustic Imaging. Interface Focus. 2011; 1:602–631. [PubMed: 22866233]
34. Li H, Dong B, Zhang Z, Sun C, Zhang HF. A transparent broadband ultrasonic detector based on micro-ring resonator for functional photoacoustic imaging. Sci. Rep. 2014; 4:4496. [PubMed: 24675547]
35. Wang Y, Wang RK. Photoacoustic recovery of an absolute optical absorption coefficient with an exact solution of a wave equation. Phys Med. Biol. 2008; 53:6167. [PubMed: 18854608]
36. Zhang Z, Dong B, Li H, Zhou F, Zhang HF, Sun C. Theoretical and experimental studies of distance dependent response of micro-ring resonator-based ultrasonic detectors for photoacoustic microscopy. J. Appl. Phys. 2014; 116:144501. [PubMed: 25378712]
37. Bauer-Marschallinger J, Berer T, Grun H, Roitner H, Reitinger B, Burgholzer P. Broadband high-frequency measurement of ultrasonic attenuation of tissues and liquids. IEEE Trans. Ultrason. Ferroelectr Freq. Control. 2012; 59:2631–2545. [PubMed: 23221212]
38. Hadimioglu, B., Khuri-Yakub, BT. Ultrasonics Symposium, 1990. Vol. 3. Proceedings., IEEE; 1990. Polymer films as acoustic matching layers; p. 1337-1340.1990
39. Hageman, GS., Gehrs, K., Johnson, LV., Anderson, D. In Age-Related Macular Degeneration (AMD). In: Kolb, H.Fernandez, E., Nelson, R., editors. Webvision: The Organization of the Retina and Visual System. University of Utah Health Sciences Center; Salt Lake City, UT: 2008.
40. Bonilha VL. Age and disease-related structural changes in the retinal pigment epithelium. Clin. Ophthalmol. 2008; 2:413–424. [PubMed: 19668732]
41. Zareba M, Skumatz CMB, Sarna TJ, Burke JM. Photic injury to cultured rpe varies among individual cells in proportion to their endogenous lipofuscin content as modulated by their melanosome content. Invest. Ophthalmol. Vis. Sci. 2014; 55:4982–4990. [PubMed: 25034597]
42. Zhang XY, Zhang HF, Puliafito CA, Jiao SL. Simultaneous in vivo imaging of melanin and lipofuscin in the retina with photoacoustic ophthalmoscopy and autofluorescence imaging. J. Biomed. Opt. 2011; 16:080504. [PubMed: 21895304]
43. Zhang HF, Puliafito CA, Jiao SL. Photoacoustic ophthalmoscopy for in vivo retinal imaging: current status and prospects. Ophthal. Surg. Las. Im. 2011; 42:S106–S115.
44. Seagle BL, Gasyna EM, Mieler WF, Norris JR Jr. Photoprotection of human retinal pigment epithelium cells against blue light-induced apoptosis by melanin free radicals from Sepia officinalis. PNAS. 2005; 103:16644–16648.
45. Bindewald-Wittich A, Han M, Schmitz-Valckenberg S, Snyder SR, Giese G, Bille JF, Holz FG. Two-photon-excited fluorescence imaging of human RPE cells with a femtosecond Ti:Sapphire laser. Invest. Ophthalmol. Vis. Sci. 2006; 47:4553–4557. [PubMed: 17003452]
46. Ling T, Chen S-L, Guo LJ. Fabrication and characterization of High Q polymer micro-ring resonator and its application as a sensitive ultrasonic detector. Opt. Express. 2011; 19:861–869. [PubMed: 21263625]

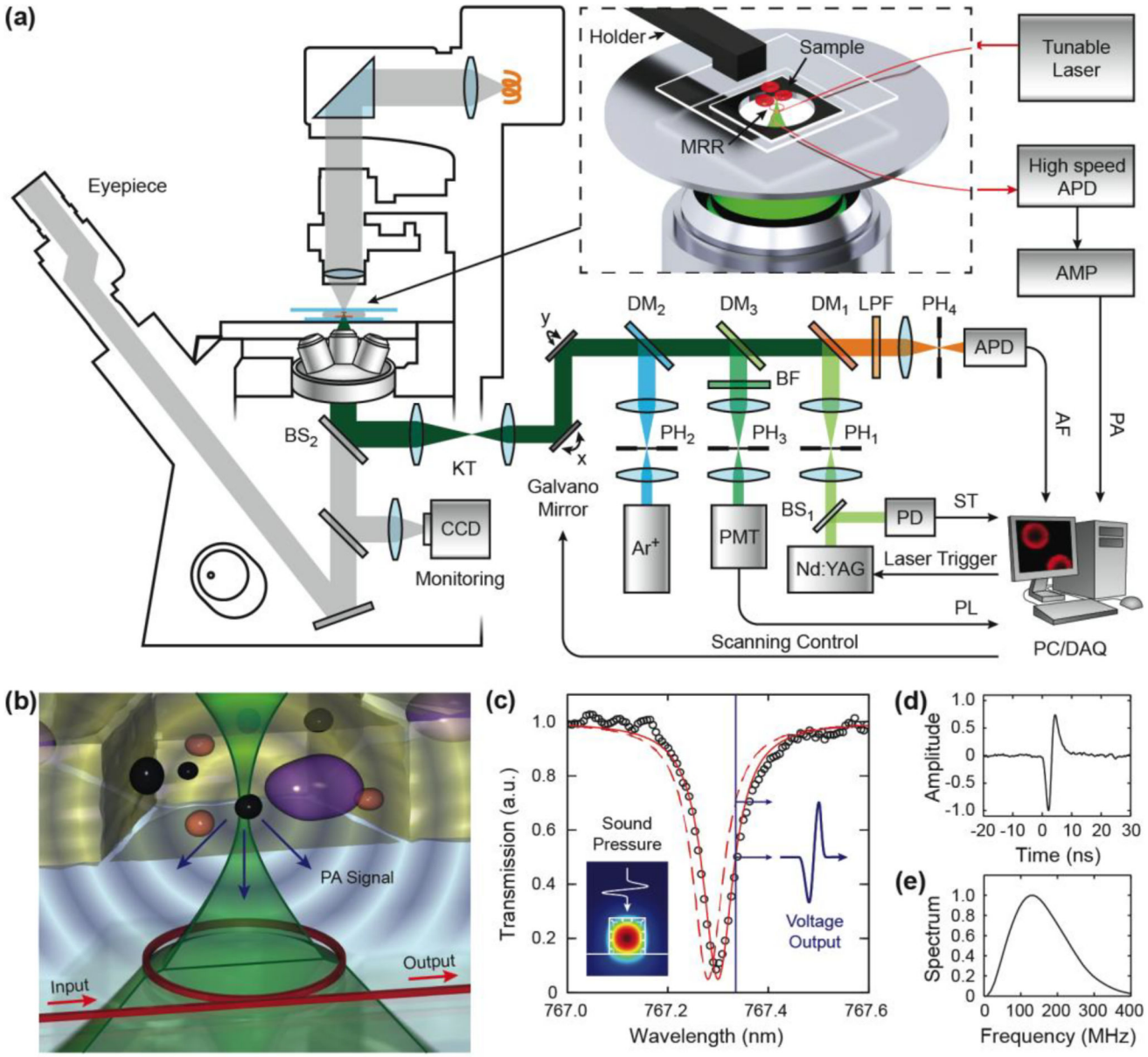

Fig. 1.

Schematic of the multimodality microscopy system. (a) An integrated microscopic system combining laser scanning confocal microscopy and PAM was realized by an optically transparent MRR ultrasonic detector. The inset illustrates a magnified view of the placement of the fiber coupled MRR ultrasonic detector and specimen. (b) Illustration of MRR detection of laser induced PA waves. (c) A representative transmission spectrum exhibits a pronounced resonance dip under the critical coupling condition (black circle) and its corresponding Lorenz fitting (red line). Inset is the numerical simulation of the electric field distribution, which shows the fundamental TM mode in the waveguide. Using a narrow-band laser source (blue line), the pressure induced resonance shift (dashed red line) can be measured as the amplitude modulation of the transmitted optical signal. (d) The time-

resolved PA pulse signal measured by the MRR ultrasonic detector. (e) Its corresponding power spectrum shows an ultra-broadband frequency response.

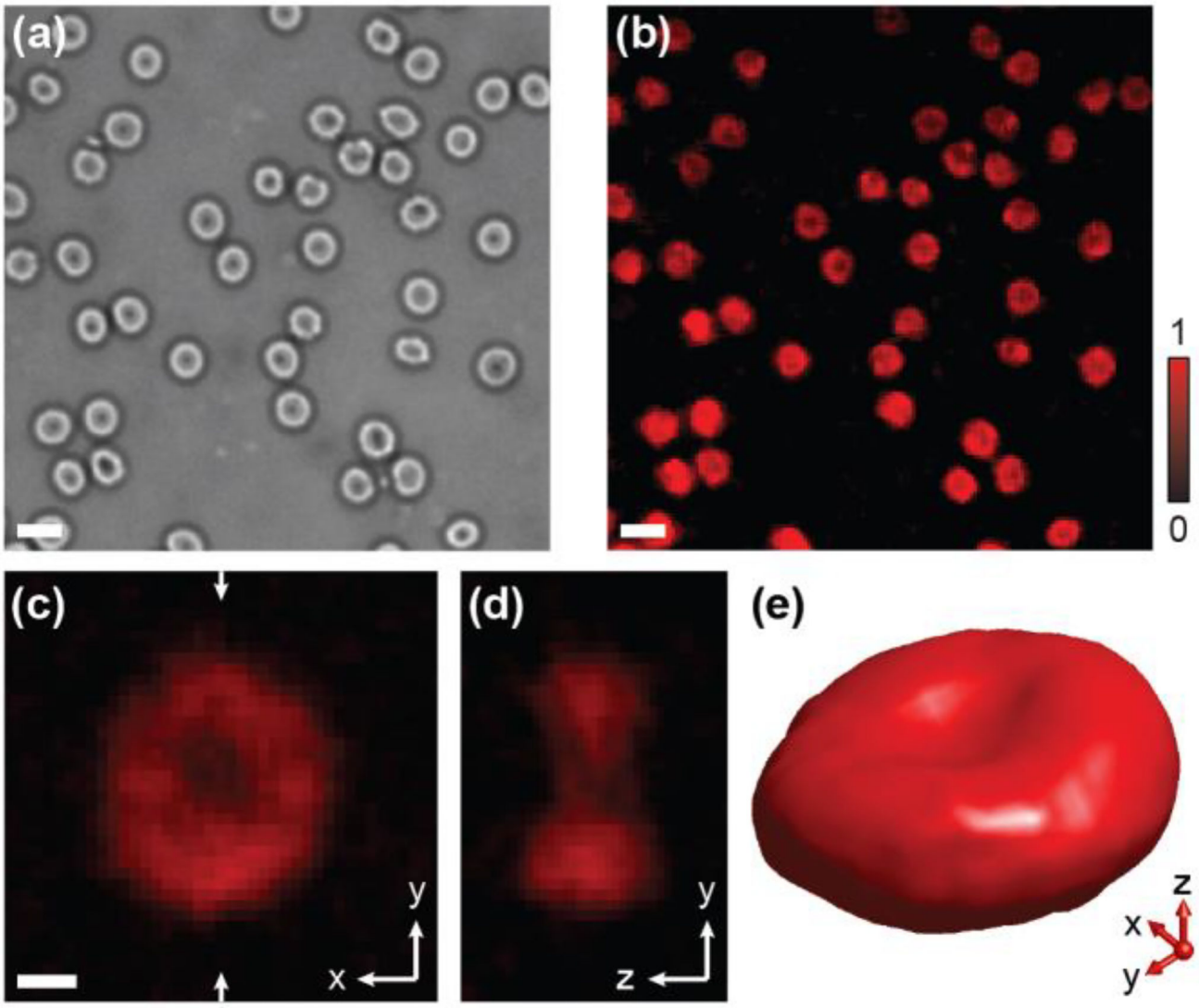

Fig. 2.

PAM imaging of single RBCs in a mouse blood smear. (a) Trans-illuminated optical microscopic image. (b) PA MAP image of individual RBCs. scale bars: 10 μm. (c) Magnified PAM projection image of a single RBC along the x-y plane; scale bar: 2 μm. (d) Cross-sectional image of the same RBC along the x-z plane. (e) 3D visualization of the RBC, a movie can be found from the supplementary material.

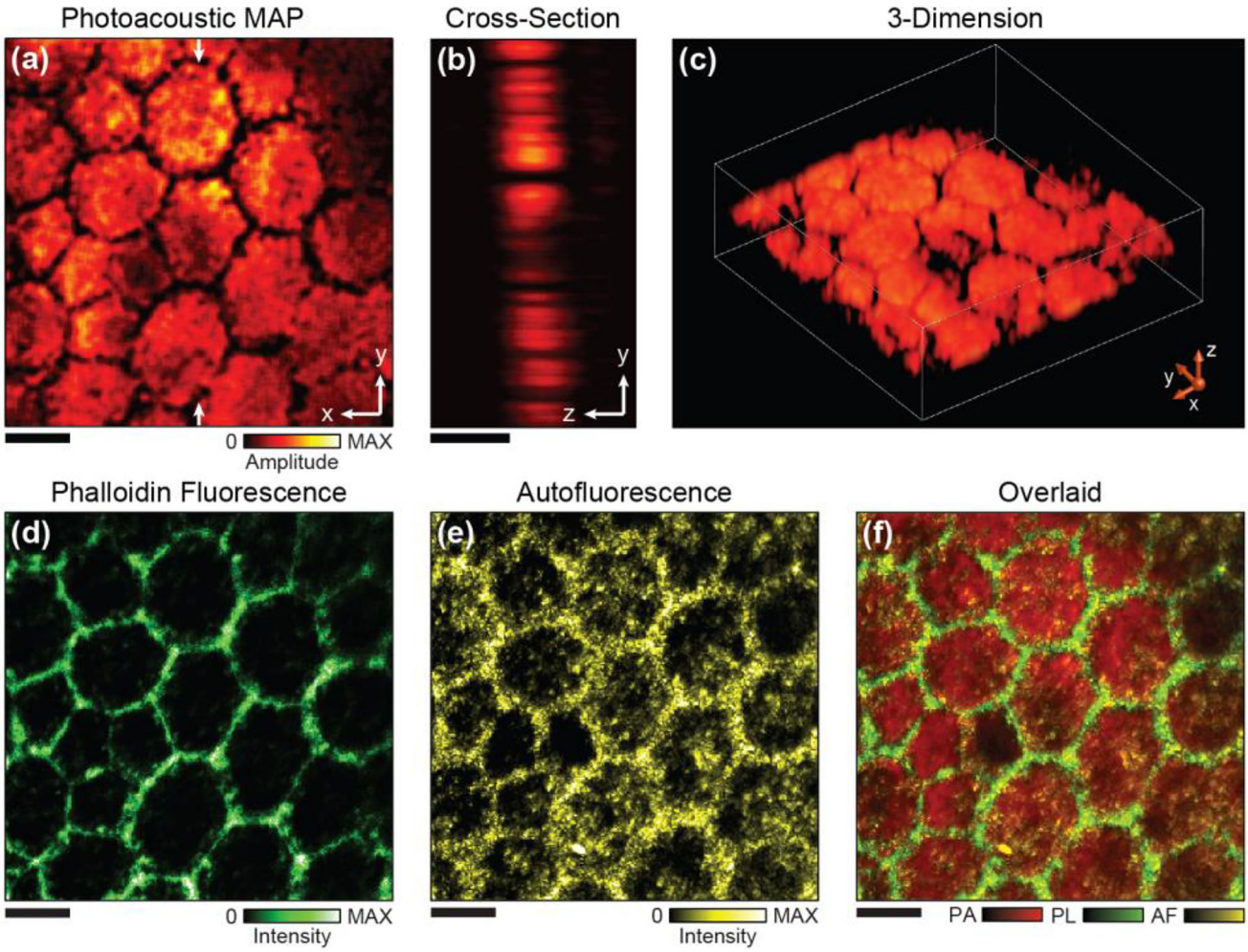

Fig. 3.

Simultaneous PAM and fluorescence confocal imaging of a human RPE flat mount. (a) Projection PAM image of the RPE along the x-y plane. (b) Cross-sectional PAM image along the x-z plane. (c) 3D visualization of the RPE cells imaged by PAM. (d) Actin stained confocal imaging highlights the boundaries of the RPE cells. (e) Autofluorescence confocal image shows the distribution of lipofuscin. (f) Overlaid image of all the three modalities acquired simultaneously. Scale bars: 10 μm.